Chapter 5

Polyaniline functionalized ECC via *in-situ* chemical polymerization for improved supercapacitor performance

This chapter deals with the synthesis of Polyaniline functionalized activated carbon obtained from bio-waste via in-situ chemical polymerization methods using ammonium peroxosulphate as an oxidant and as-synthesized materials are well characterized. This hybrid is used as electrode material for supercapacitor.

5.1 Introduction

In recent years, there has been growing attention in waste management systems as the recycling of waste materials into useful materials. Significant researches have been done so far to reuse and recycle organic waste (that is also called bio-waste) into various porous carbonaceous materials [Ahammad et al. (2019), Shah et al. (2019), Buliyaminu et al. (2020), Deb et al. (2019)]. Additionally, such carbonaceous materials possess unique surface structures, feasible cost, chemical inertness, high surface area, and synthetically tunable electrical, optical and thermal properties. Therefore, these kinds of materials are presently preferred as the electrode materials for the supercapacitor applications [Sevilla et al. (2014), Biswal et al. (2013)]. Carbonaceous materials exhibit capacitive behavior mainly through the Electrolytic Double-Layer Capacitor (EDLS) in which the charge/ions are stored followed by the non-faradic process at the electrode-electrolyte interface. But lack of redox centers, the intrinsic grain-boundary and scattering of charge carriers are some issues related to the carbon materials which deteriorate/limit their specific capacitance as well as the charge transport properties [Goswami et al. (2019)]. To overcome the aforementioned concerns, researchers started to embed some redox-active components within carbon nanomaterials considerably but still are subject to challenge and criticism. CPs and metal oxides are the most common redox-active materials and are frequently used in the preparation of various composite/hybrid electrode materials. Based on this, numerous kinds of hybrids including carbon nanomaterials associated with the redox components e.g. metal oxides as well as CPs are reported having improved electrochemical properties. Eskusson et al. (2016) published Fe_3O_4-graphene

nanocomposite, Deng et al. (2017), Luo et al. (2017), Pandit et al. (2019) reported carbon nanotube (CNT)/cerium-oxide nanocomposite for supercapacitor application. Wang et al. (2019) synthesized CuO_x/porous carbon hybrid, Wu et al. (2010), and Chauhan et al. (2016) synthesized graphene/PAni nanocomposites, Zhang et al.(2010) prepared uniform PAni fibers coated graphene nanocomposite and discussed in details about the influence on their electrochemical performance, Hong et al. (2019) reviewed on graphene/PAni nanocomposites for supercapacitor, Goswami et al. (2019), published work based on biowaste-derived carbon black/Polyaniline composites high-performance supercapacitor microelectrodes. Shah et al. (2019) worked on polyaniline and heteroatoms–enriched carbon derived from Pithophorapolymorpha as efficient electrode material for supercapacitor. The presence of nanostructured metal oxides as well as CPs can improve the redox and transport properties and results in enormous improved supercapacitive performance compared to the bulk materials. Among them, CPs has drawn great attention for present research because of their low cost, ease in synthesis, range of flexibility, functionality, tunability and good electrical conductivity [Kulkarni et al. (2014), Shah et al. (2020), Zhang et al. (2018)]. Notably, CPs such as polyaniline (PAni), Polyindole (PIn), polypyrrole (PPY), polythiophene (PT) and Polycarbazole (PCz) possess excellent conducting properties as well as high pseudocapacitance, and have been widely used for electrochemical applications [Zhang et al. (2018), Li et al. (2009]. Especially, PAni has been aroused as the most promising pseudocapacitive materials to fabricate composites with the carbonaceous materials [Snook et al. (2011)]. Because PAni being an organic conductor by way of easy synthesis and

manipulation, low-cost monomer, excellent energy storage capacity, biocompatibility, interesting doping chemistry, good environmental stability, high conductivity/electro-activity etc [Dhand et al. (2011).

Keeping all these points in mind, present chapter is focused on the modification or embedded the PAni with ECC (ECC is a carbonaceous material as discussed in chapter 4). Aiming to enhance the supercapacitor performance of carbonaceous material, the general method for surface modification of the ACs material is done as following steps. Before modification, oxidation of ECC 800 using acid HNO_3has performed first which is denoted as Ox-ECC and then followed by PAni coating (denoted as Ox-ECC/PAni). HNO_3 treatment is the most usual method for carbon surface oxidation [Moreno-Castilla et al. (1996)], where the aliphatic chains are oxidized, but the aromatic rings are not affected because of the high stability of aromatic rings. This process creates additional oxygen functionalities that improve the surface area, hydrophilicity which favoring for the larger electrolyte interactions and enhancing its electrochemical performance of supercapacitors [Jin et al. (2013)]. Furthermore, HNO_3 treatment not only improve the specific capacitance, but impacted in their cyclability also.

The insertion of conducting polymers between the carbon sheets is one logical and convenient option to promote the transportation of electrolyte ion that results in enhanced performance and electrical conductivity [Singh et al. (2013)]. PAni is well known organic semiconducting conducting polymer and able to transport charges by the means of the delocalization process [Liu et al. (2012), Wang et al. (2012)].Our purpose is to shorten the charge transport path length of defective ACs surface. That

is why; we tried to make a thin layer of PAni over the oxidized ECC 800 (Ox-ECC) (*See* Figure 5.1). The structural identification of such modified material has carried out using various techniques like Powder X-Ray diffraction (XRD), Fourier-transform infrared spectroscopy (FT-IR), Raman and Field Emission Scanning Electron Microscopy (FE-SEM), Transmission electron microscopy (TEM) and X-ray photoelectron spectroscopy (XPS). Surface areas of all samples have been investigated under BET analysis. Furthermore, the electrochemical performances of the as-synthesized nanohybrids have been conducted for their supercapacitive behavior using Nafion as a binder and activated acetylene black as a conductive component. A good agreement is observed as per our expectation with good relation between morphological characterizations and electrochemical performances.

5.2 Materials and methods

5.2.1 Materials

ECC800 used here is prepared as in our earlier chapter 4. Aniline monomer, ammonium peroxodisulphate, APS ($(NH_4)_2S_2O_8$, potassium bromide (KBr), sulphuric acid (H_2SO_4), and nitric acid (HNO_3) purchased from Merck, India and used as received. Ultrapure water used here was collected from CIF, IIT (BHU).

5.2.2 Synthesis of Ox-ECC800

For oxidation of as-prepared AC at 800^oC (as discussed in chapter 4), nitric acid treatment was performed. In this process, 100 mg ECC 800 powder was mixed with 50 mL of 5 M HNO_3 solution in a 100 mL glass beaker and sonicated for 30 min. After that, the above reaction mixture was continuously stirred at 90^oC for 3h and

then cooled to room temperature. Finally, the oxidized AC powder was separated, washed several times with ultrapure water until pH=7 and dried in a vacuum oven at 100^{o}C for overnight.

5.2.3 Synthesis of PAni and Ox- ECC 800/PAni

PAni was synthesized using the *in-situ* chemical oxidation of aniline monomer with some modification [19-20]. Briefly, 2 mL of aniline was added into 5 mL of 1M H_2SO_4 solution at low temperature (ice-bath) under constant stirring condition. Thereafter, polymerization was started by adding the oxidant solution APS ($(NH_4)_2S_2O_8$ 2g in 15mL 1MH_2SO_4), drop by drop into the above monomer solution. The reaction mixture was left as such for 4 h under constant stirring and subsequently put into the freeze for 24h. After polymerization, a dark green color precipitate obtained was separated, washed with ultrapure water and ethanol, and dried in a vacuum oven at 80 °C for 10 h.

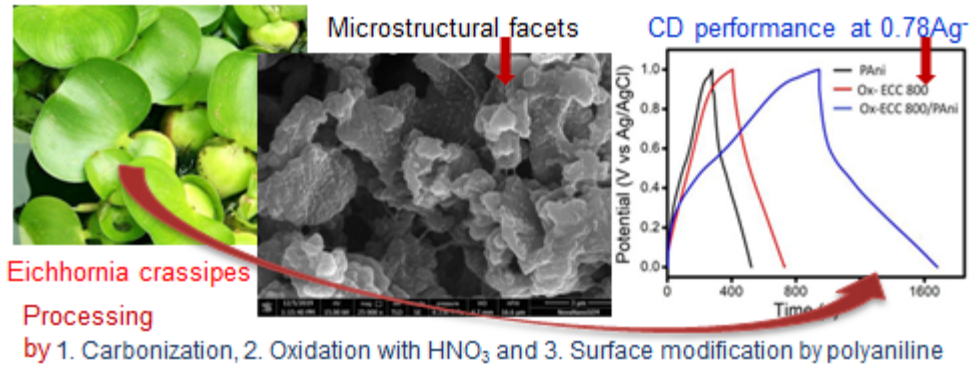

Figure 5.1 Schematic representation of ECC surface modification with PAni

Ox-ECC/PAni is synthesized by the *in-situ* polymerization process of aniline over Ox-ECC surface. In this process, a dispersion of 40 mg Ox-ECC in 5 mL of 1M

H_2SO_4 was prepared, and then 100µL aniline was added dropwise to above dispersion followed by constant stirring for 30 minutes. After that, polymerization was carried out by the dropwise addition of the APS solution (100 mg in 2mL of 1M H_2SO_4). Hybrid was collected by a similar protocol as described for PAni.

5.2.4 Modification of Working Electrode

Modification of Working Electrode has been done by a similar protocol as described for earlier chapter 4.

5.3 Results and discussion

The graphitization of carbon skeletons at elevated temperatures leads to the generation of various bonding interactions such as π-π interaction (between inter/intra sheet's aromatic rings), H-bonding or electrostatic interactions (among available functional groups) etc. Such interactions lead to a direct improvement in the charge conduction path. However, very high synthetic temperature and/or post-synthetic chemical treatment create defect(s) on graphitized surfaces and consequently locally imped the charge conduction. Therefore, incorporation of conducting and functional polymers not only enhances the aforesaid interactions but also induces covalent bond linkages that can reduce internal resistance in such kind of defective materials. For example, anchoring of PAni wires, covalent bond linking of PAni with graphene oxide as phenazine or phenoxazine linkage is able to improve charge storage and/or conduction path [Liu e al. (2012), Wang et al. (2012), Zhong et al. (2012)]. In view of the above facts, we are trying to establish such kinds of interactions between ECC 800 and PAni that is eligible to exhibit better charge storage as discussed later.

5.3.1 Structural analysis

XRD spectra:

Except for a few remarkable observations, Ox-ECC is exhibiting an almost similar diffraction pattern as observed for ECC 800 (*cf*. Figure4.2 c with Figure 5.2a)[Zhang et al. (2018), Biswal et al. (2013) , Shang et al. (2015) , Subramaniyam et al. (2017) , Wang et al. (2018)]. Similarly, PAni is exhibiting its characteristics peaks at $2\theta=16^{o}$, 21^{o}, 25.5^{o} and 27^{o} due to periodicity parallel to the periodic chain and periodicity perpendicular to the periodic chains (Figure 5.2c) [Liu et al (2012), Wang et al. (2012)]. In the case of Ox-ECC/PAni, the XRD pattern consists of peaks related to both components of Ox- ECC 800 and PAni (Figure5.2b). It means that Ox- ECC 800 is not destroying its identity and polymerization of aniline to PAni occurs successfully even in the presence of Ox- ECC 800 dispersion. The peak intensity of 25.5^{o} (for (002 planes) is enhanced in the case of Ox-ECC/PAni as compared to those of Ox-ECC and full-width half maxima are reduced (*cf*. Figure 5.2a with Figure 5.2b) which indicate the existence of π-π interaction between Ox-ECC800/PAni [Wu et al. (2019)].

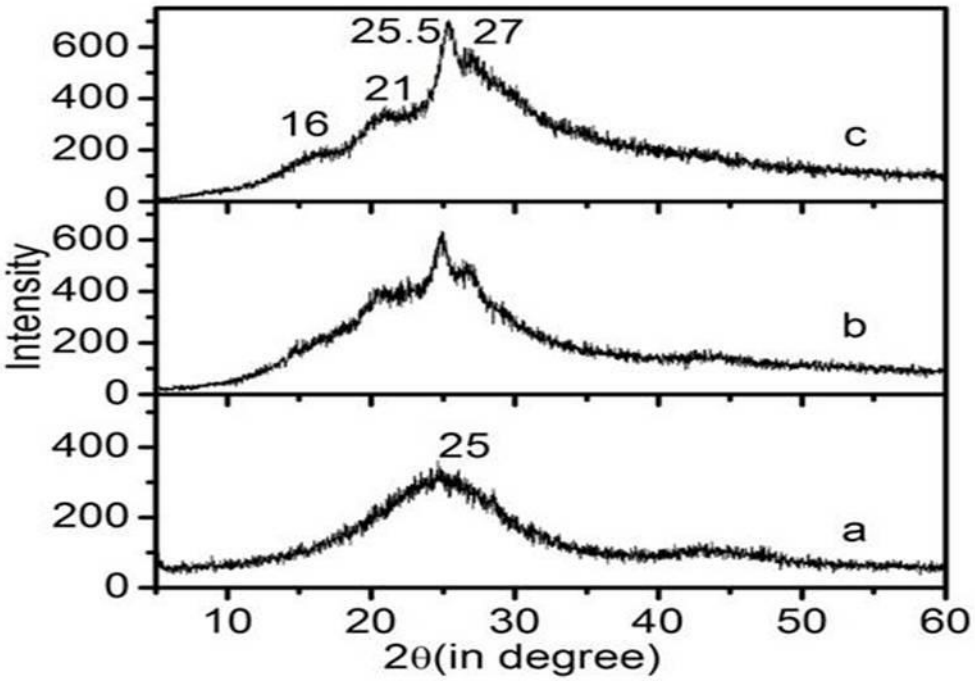

Fig. 5.2: (I) XRD of (a) Ox- ECC 800, (b) OX-ECC/PAni and (c) PAni.

FT-IR analysis:

FT-IR analysis of Ox-ECC, PAni and Ox-ECC/PAni were carried out in order to get the different functionalities (as shown in Figure 5.3). Ox-ECC (*See* Figure 5.3a) is exhibiting similar kinds of functionalities as ECC (discussed in chapter 4) with slight variations and attribute to –OH hydroxyl groups, C=C stretching vibrations of an aromatic ring, which justifies the π-conjugated sp^2-hybridized system. Broadband in range ~1010–1100 cm^{-1} indicates the presence of the C–O bond of alcohols, carboxylic acids, phenols and esters [Inala et al. (2018)]. The FT-IR spectrum PAni showing vibration peaks at 1474 cm^{-1} and 1561 cm^{-1} due to the benzenoid ring and quinoid ring skeletons respectively. The broad vibration peak at 3439 cm^{-1} is ascribed to the N–H stretching mode. The other vibration bands at 1235, 1294 cm^{-1}, 1118 cm^{-1}

and 800 cm^{-1} are associated with the C–N stretching of the secondary aromatic amine, aromatic C–H in-plane bending and out-of-plane bending vibration respectively (Figure 5.2c) [Wu et al. (2019), Khalili et al. (2016)]. However, Ox-ECC/PAni is showing all aforesaid characteristic peaks related to Ox-ECC and PAni components. For example, the broad vibration peak at 3425 cm^{-1} is assigned to the N–H stretching mode from the PAni. The vibration peaks at 1493 cm^{-1} and 1576cm^{-1} are due to the benzenoid ring and quinonoid ring vibrations, respectively. Other vibration bands at 1231 cm^{-1} is associated with C–N stretching. The vibration peak corresponding to aromatic C–H in-plane bending is shifted to 1168 cm^{-1} from 1118 cm^{-1}, suggesting an interaction between ECC 800 and PAni (Figure 5.3b) [Elnaggar et al. (2017)]. The vibration peak at 1049 cm^{-1} is attributed due to SO_4^{2-} dopant ion in the polymer backbone.

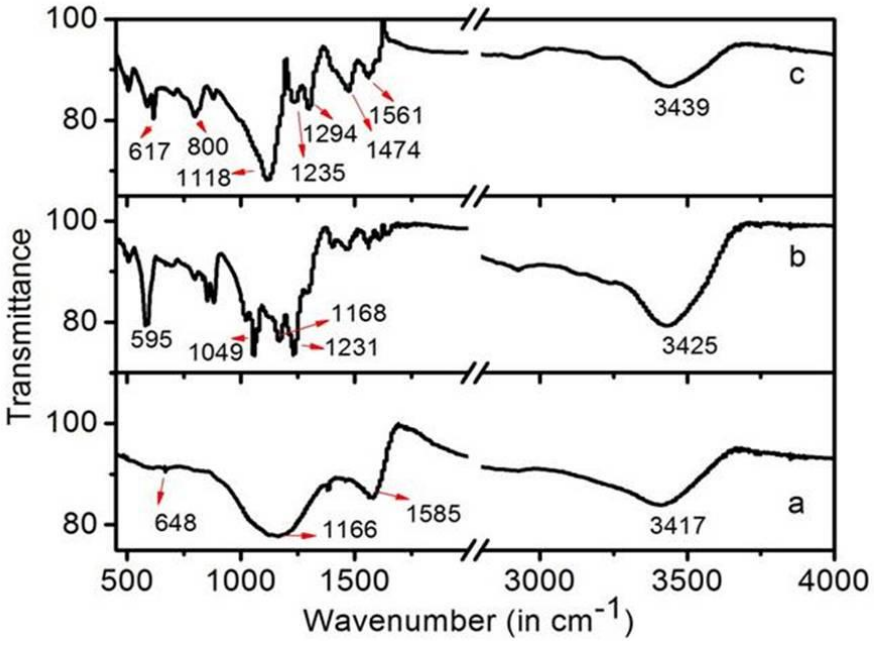

Figure 5.3 FT-IR analysis of (a) Ox- ECC 800, (b) OX-ECC/PAni and (c) PAni.

Raman analysis:

Raman spectroscopy was used to confirm the disorderness of graphitic domains in Ox- ECC 800, OX-ECC/PAni and PAni (as shown in Figure 5.4). Both ECC 800 (used in chapter 4) and Ox-ECC are showing two characteristics peaks centered at 1316 cm^{-1} and 1600 cm^{-1} due to so called D-and G-band associated with disordered carbon and in-plane vibration of graphitic domain respectively (*cf.* Figure 4.3II and Figure 5.4a). On comparing the I_D/I_G ratios of Ox-ECC and ECC 800, the I_D/I_G ratio of Ox-ECC increased to 1.43 from 1.33 (ECC 800) due to an increase in the disorderness [Subramaniyam et al. (2017), Jin et al. (2013)]. PAni exhibits all characteristics peaks which are similar and in good agreement with previous work indicating the existence of bending and stretching vibrations of benzenoid and quinoid units [Alas et al. (2019), Wang et al. (2015)]. The Raman band from 300-1000 cm^{-1} range exhibits the information about benzene ring deformations. The band at 412, 580, and 809 cm^{-1} are associated with out-plane and in-plane vibrations of protonated emeraldine form of the polymer [Sawangphruk et al. (2013)]. Similarly, the Raman band at 1165 cm^{-1} (C-H bending), 1250 cm^{-1} (C-N stretching), 1331 cm^{-1} ($C\text{-}N^+$ stretching), 1499 cm^{-1} (C=N stretching vibration of benzenoid), 1582 cm^{-1} (C=C stretching vibration of benzenoid), 1616 cm^{-1} (C=C stretching of the quinoid ring) are associated to different available functionalities of PAni (Figure 5.4c) [Dennany et al. (2011), Goswami et al. (2019)]. However, in Ox-ECC/PAni, all Raman bands corresponding to PAni is dominated across the background band of Ox-ECC (*See* Figure 5.4b). These observations indicate that the wastes derived carbon Ox-ECC is well-connected to the PAni and results Ox-ECC/PAni.

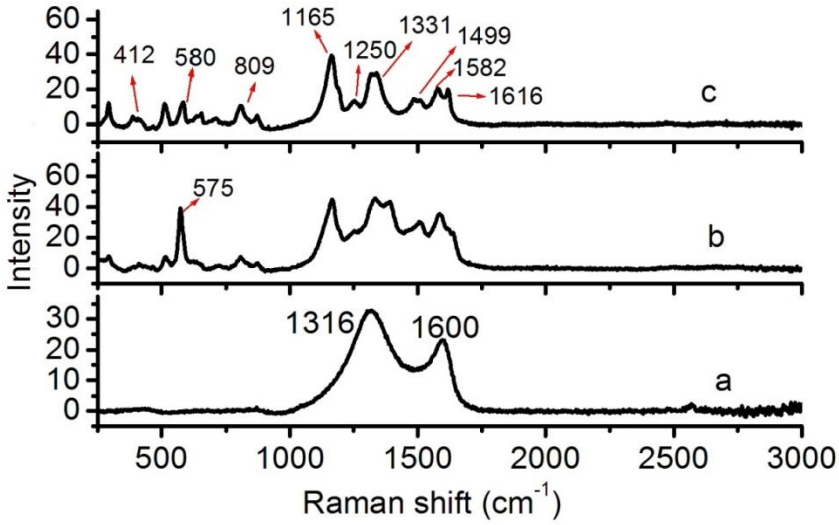

Fig. 5.4 Raman of (a) Ox-ECC, (b) Ox-ECC/PAni and (c) PAni.

XPS analysis:

To find out the chemical compositions and their bonding environment of the elements in Ox-ECC and Ox-ECC/PAni, XPS was performed (as shown in Figure 5.5). XPS survey spectra of both samples gave clear evidence for the existence of three elements carbon, nitrogen and oxygen (Figure 5.5a and 5.5b). Factually, carbon-based materials having heteroatoms (like O and N) provides a positive center which can offer better electrochemical capacitive performance [Hoang et al. (2020)]. For more details, we deconvoluted each peak separately. After deconvolution, it is observed that C1s peak of the Ox-ECC is disassembled into three peaks at 284.6eV, 286.2eV and 288.8eV corresponding to the signal of C=C-C bonds, C–N/C–O and O–C=O bonds respectively (Figure 5.5 c) [Hoang et al. (2020)]. The N1s spectrum also has three subpeaks as for –N= (imine nitrogen) at 398.4eV, pyrrolic at 400.6eV which are so called active center for electrochemical reactions, and quaternary nitrogen at 403.7eV (Figure 5.5e) [Zhou et al. (2014)].Similarly, the O1s spectrum exhibits peaks

for three different oxygen moieties at binding energy 531.3eV, 533.4eV and 535.6eV corresponding to H–O–C/O–O–C,–COOH carboxyl groups and O=C, and chemisorbed oxygen respectively (Figure 5.5g) [Oh et al. (2014)]. On the other hand, XPS spectrum of Ox-ECC/PANI corresponding to C1s showing four peaks at 284.6eV, 285.4 eV, 286.7eV and 288.2eV for C=C-C (graphitic) bonds, C=C (quinoid part of PAni), C–N/C–O and O–C=O bonds respectively (Figure 5.5d). N1s has four peak at 399.01eV, 399.7eV, 400.7 eV and 401.8eV due to –N= (imine), –NH-, $–NH^{+}$ and $=NH^{\cdot+}$(Figure 5.5f) [Cho et al.(2013)]. Similarly, O1s exhibit four peaks at 530.9eV, 531.4eV, 532.1eV and 533.2eV due to quinone-type groups, C=O, C-O-C and C-O-H respectively [Figure 5.5h]. These observations were in consistent with the speculations based on the results of FT-IR and Raman.

5.3.2 Morphological analysis:

In order to assess the morphology and microstructure of as-prepared three samples, SEM imaging was captured (Figure 5.6). The morphological texture of Ox-ECC is showing almost a similar trend as in ECC 800 (*cf.* Figure 4.4c and Figure5.6a). However, we observed differences in processability and BET surface area due to available functionalities after oxidation (discussed later). PAni has an inhomogeneous globular shape that is fused (Figure 5.6b). However, in the case of Ox-ECC/PAni (Figure 5.6c), the respective microstructure showing PAni globules over the Ox-ECC sheets. This microstructure is evidencing the co-existence of both the OX-ECC and PAni without any disruption during composite formation.

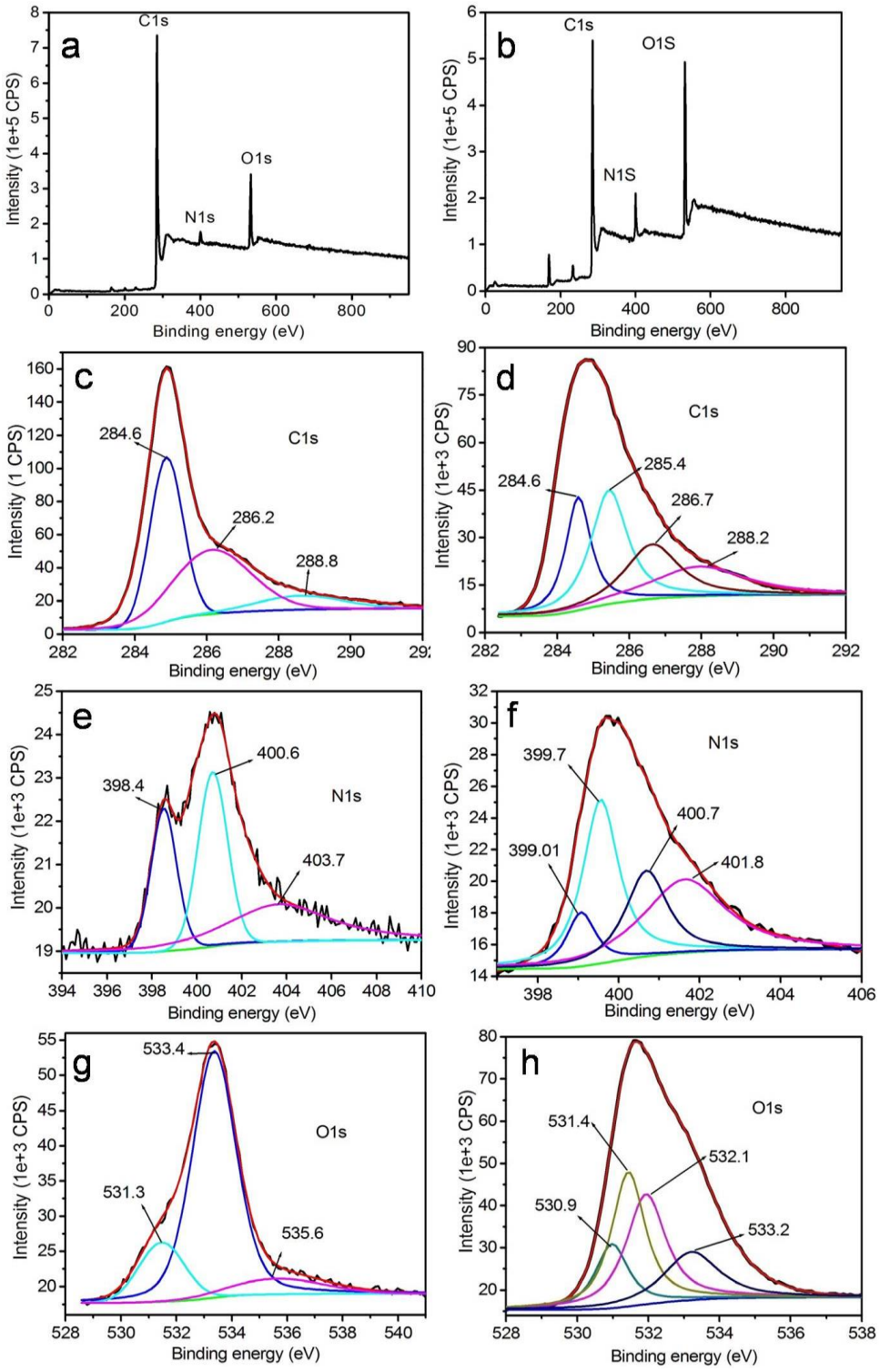

Fig.5.5 XPS of Ox-ECC for (a) survey spectrum, (c) C_{1s}, (e) N_{1s}(g) $O_{1s}$and Ox-ECC/PAni for (b) survey spectrum, (d) C_{1s}, (f) N_{1s} (h) O_{1s} respectively.

For the more exemplified the microstructure of Ox-ECC/PAni, TEM experiment was performed. Based on TEM micrographs, it can be seen that the OX-ECC sheets are crimped together and PAni coating exists over these sheets confirming our claim of surface modification (Figure 5.6d and Figure 5.6e).

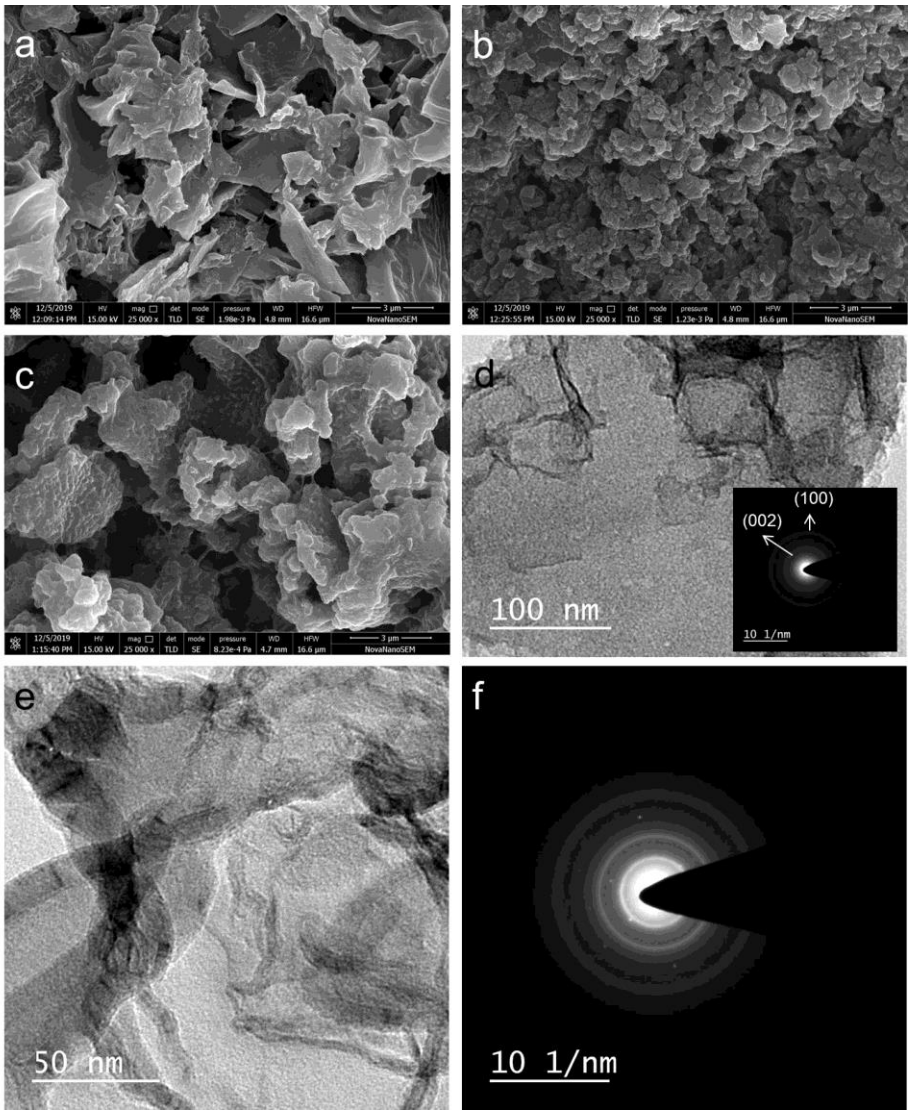

Figure 5.6: SEM image of (a) Ox-ECC (b) PAni, (c) Ox-ECC/PAni, TEM image of (d) Ox-ECC, (e) Ox-ECC/PAni and (f) SAED of Ox-ECC/PAni. Inset of Figure. 5.6d showing SAED of Ox-ECC.

SAED pattern of Ox-ECC (*see* inset Figure 5.6d) is exhibiting diffraction pattern close to that of graphitic carbons and showing diffraction pattern corresponding to (002) and (100) planes, however, SAED pattern of Ox-ECC/PAni (Figure 5.6f) showing a set of concentric rings corresponding (010), (100) and (110) crystalline planes of PAni, respectively. These results are also supportive of our XRD data.

5.3.3 BET Surface area analysis:

In order to inspect the surface area and the porosity of as-synthesized Ox-ECC, PAni, and Ox-ECC/PAni, BET N_2 adsorption/desorption isotherms were carried out to and presented in Figure 5.7. The Ox-ECC has characteristics type IV isotherms with H4 hysteresis loop which is shown in figure 5.7a, indicating a similar nature as ECC 800 (According to IUPAC as discussed in chapter 4). The initial part of the adsorption-desorption isotherms is showing a significant N_2 gas uptake at low relative pressures which correspond to the micropores structure and a hysteresis loop at higher relative pressures accompanying the existence of a mixture of microporous and mesoporous structures [Madhu et al. (2014), Wahid et al. (2014), Kumar et al. (2016)]. Acid treated Ox-ECC exhibits slightly low surface area value than ECC 800 (781 m^2g^{-1} *vs.* 713 m^2g^{-1}) due to the intercalation of more functionalities that collapses most of the pores/or partial blockage micropores (*cf.* Figure 5.7a and Figure 4.5c) [Jaramillo et al. (2010), Moreno-Castilla et al. (1996]. In the case of PAni, the corresponding N_2 adsorption/desorption isotherms have characteristics type III isotherms which is shown in figure 5.7b. This isotherm adsorbed at high relative pressure ~ 1.0 (>0.9) reveals the existence of macropores. Due to the compact nature of PAni, it exhibits the lowest value of surface area 36.5m^2g^{-1} than other materials. Ox-ECC/PAni also

following the similar pattern as Ox-ECC, and suggesting for a meso-/micro-pores structure that offers diffusion channels for electrolyte-ion, and recommend the space for ion storage [Bi et al. (2019)]. However, in the case of Ox-ECC/PAni, the adsorption of nitrogen decreases and hence surface area reduces to 316 m^2g^{-1} from 713 m^2g^{-1} due to polymer coating that reduces the pores of Ox-ECC (Figure 5.7 c). The pore sizes and pore volume of these samples are estimated and summarized in Table 5.1.

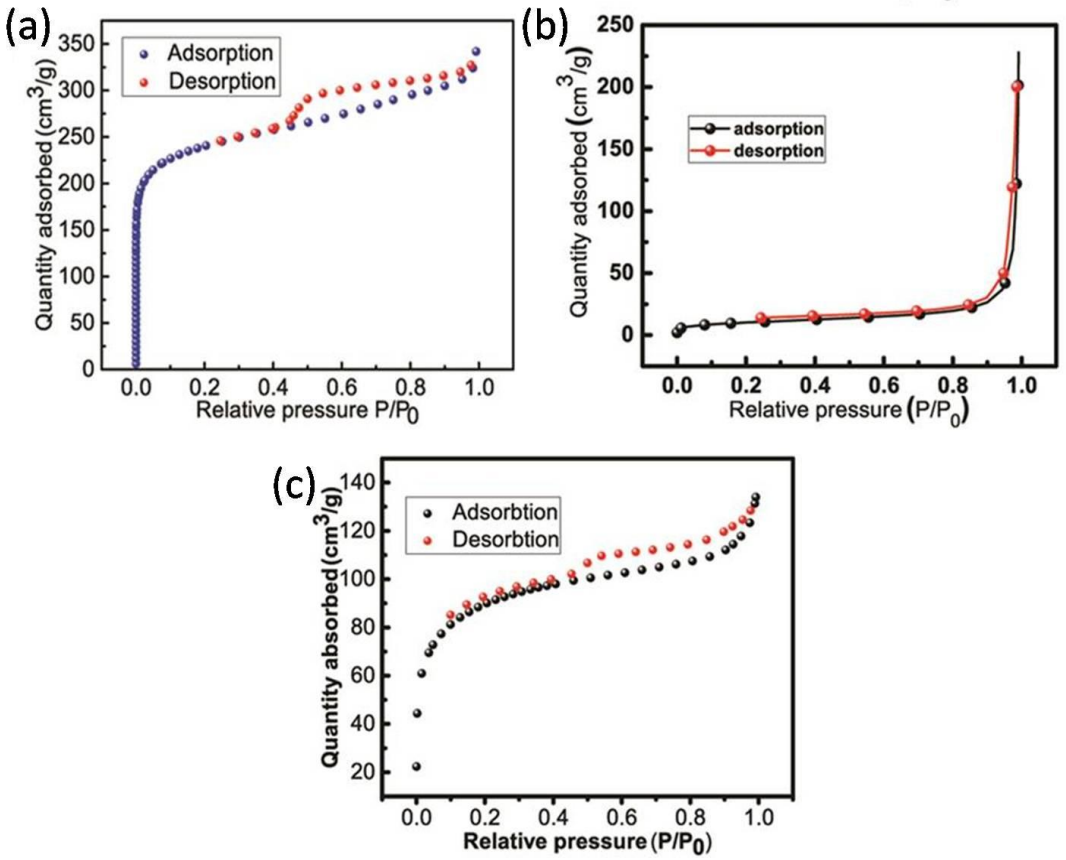

Figure 5.7 N_2 adsorption-desorption isotherm of (a) Ox- ECC 800, (b) PAni and (c).OX-ECC/PAni.

Table 5.1 Estimated BET surface area and other parameters for as-synthesized samples.

Sample	BET surface area (in $10^2 m^2 g^{-1}$)	Pore volume (in $cm^3 g^{-1}$)	Pore diameter (in nm)
Ox-ECC	7.13	0.35	2.26
PAni	0.36	0.29	22.1
Ox-ECC/PAni	3.16	0.21	2.59

5.3.4 Thermal analysis

The temperature sustainability of Ox-ECC, Ox-ECC/PAni, and PAni was investigated by TGA which is shown in Figure 5.8. In order to understand the effect of the functionality on temperature sustainability of materials, first, a comparative data of Ox-ECC and ECC 800 have been shown in figure 5.8I and subsequently with PAni as Figure 5.8II. On oxidation of ECC 800 with HNO_3 (Ox-ECC), the burn-off temperature further increases from 522°C to 564°C (*see* Figure 5.8I). This is due to the electrostatic interaction of available functional groups in Ox-ECC.

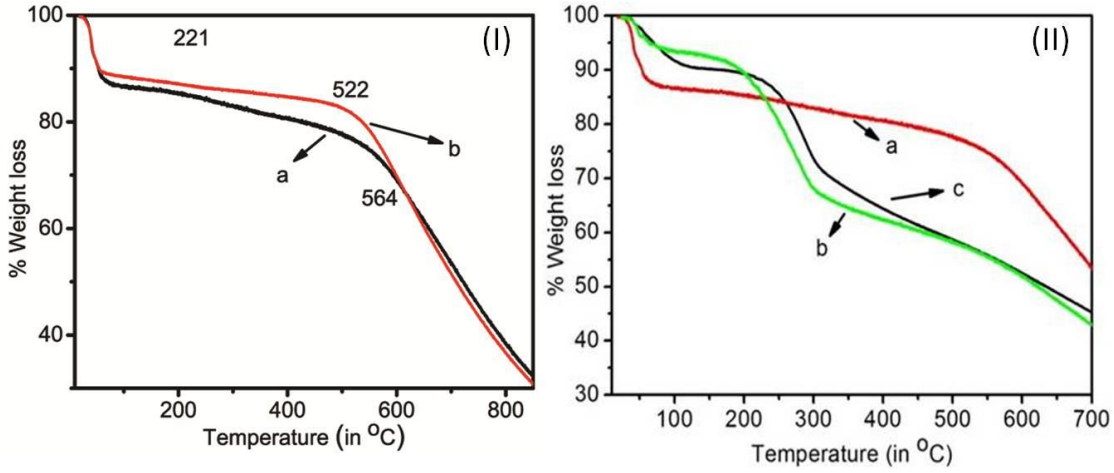

Figure 5.8 Comparative TGA of (I) (a) Ox-ECC (b) ECC 800, and (II) (a) Ox-ECC, (b) Ox-ECC/PAni, and (c) PAni.

Further, the Ox-ECC exhibits a mass loss below 100^{o}C is due to moisture and then gradual mass loss due to the decomposition of carbon (*see* Figure 5.8a). PAni is also exhibiting moisture removal below 110^{o}C, thereafter, a sharp decomposition at 244^{o}C is observed due to the decomposition of polymer backbones [Bhattacharya et al. (2014)] and further continuous degradation of these fragmented chains (Figure 5.8c). However, Ox-ECC/PAni is showing the first degradation due to moisture removal below 110^{o}C and then degradation of polymer chain occurs from the surface of ECC 800 sheets. Thereafter, the thermogram curve becomes parallel to the curve of Ox-ECC after 304^{o}C (Figure 5.8b). It means that carbon participates in thermal degradation after this temperature. Herein, we observed that PAni chains coated over Ox-ECC undergo degradation at a lower temperature (200^{o}C) [Kumar et al. (2012)] compared to that of bulk PAni (244^{o}C). It may be due to a lower extent of interchain interactions and chain entanglement in the low content of PAni coated over Ox-ECC compared to that of bulk PAni.

5.3.5 Electrochemical analysis:

CV, GCD, and EIS techniques were used in order to investigate electrochemical performance of our samples. According to the comparative CV data as (Figure 5.9Va-b), the current density response and the CV loop area of the Ox-ECC electrode are much larger, which evidently indicate that the electrochemical performance of the Ox-ECC is remarkably enhanced owing to the addition of a heteroatoms (HNO_3 treatment) [Jin et al. (2013)]. Ox-ECC exhibits better processablity and charge storage property than ECC 800 (*See* chapter 4). As Figure 5.9I, the CV of PAni exhibits irreversible redox phenomenon and area under the curve increasing on the increase in

scan rate from 20 to 150mV/s [Shah et al. (2020). This observation is implying a facile and quick adsorption and desorption of the electrolyte ions onto the working electrode [Purkait et al. (2017), Razmjooei et al. (2017), Liang et al. (2014), Biswal et al. (2013)]. The faradic oxidation-reduction peaks for PAni due to leucoemeraldine-to-emeraldine transition, is suggesting pseudocapacitive behaviour [Goswami et al. (2019)]. At the same time, its consecutive redox potentials shifted to the higher side on increasing the scan rate (Figure5.9I). It means that electrode material has low resistance and charge transport occurs via a diffusion-controlled process. Similar behaviors of the CV loop area or CV area under curves at various scan rate are also observed in the case of Ox-ECC (Figure5.9II) [Shah et al. (2020)]. As can be seen in Figure5.9II, there was no redox peak originating from the Ox-ECC electrode, it means the Ox-ECC relies the charge storage via EDLC. Similarly, except baseline shifting of the CV curve, Ox-ECC/PAni (shown as Fig 5.9III) is also exhibiting the same kind of properties as observed in the case of its parental counterparts. This shifting of the baseline is due to a change in electrical flux density, which occurs on increasing the scan rate. On comparing the CV of all samples at the same scan rate as in Figure 5.9IV, Ox-ECC/PAni is showing relatively higher area under the CV curve and current density than PAni or Ox-ECC (Figure 5.9IVa,b,c). This is due to the combined effect of Ox-ECC and PAni, in which PAni can reduce the charge conduction path length of defective Ox-ECC and also allows charge conduction by the diffusion-controlled process. To further understand the electrode reaction kinetics, a plot of current density *vs.* scan rate observed a linear behavior using

Randles−Sevcik equation as shown in Figure (Figure 5.9VI) suggesting that electrode reaction is governed under diffusion-controlled process [Piriya et al. (2018)].

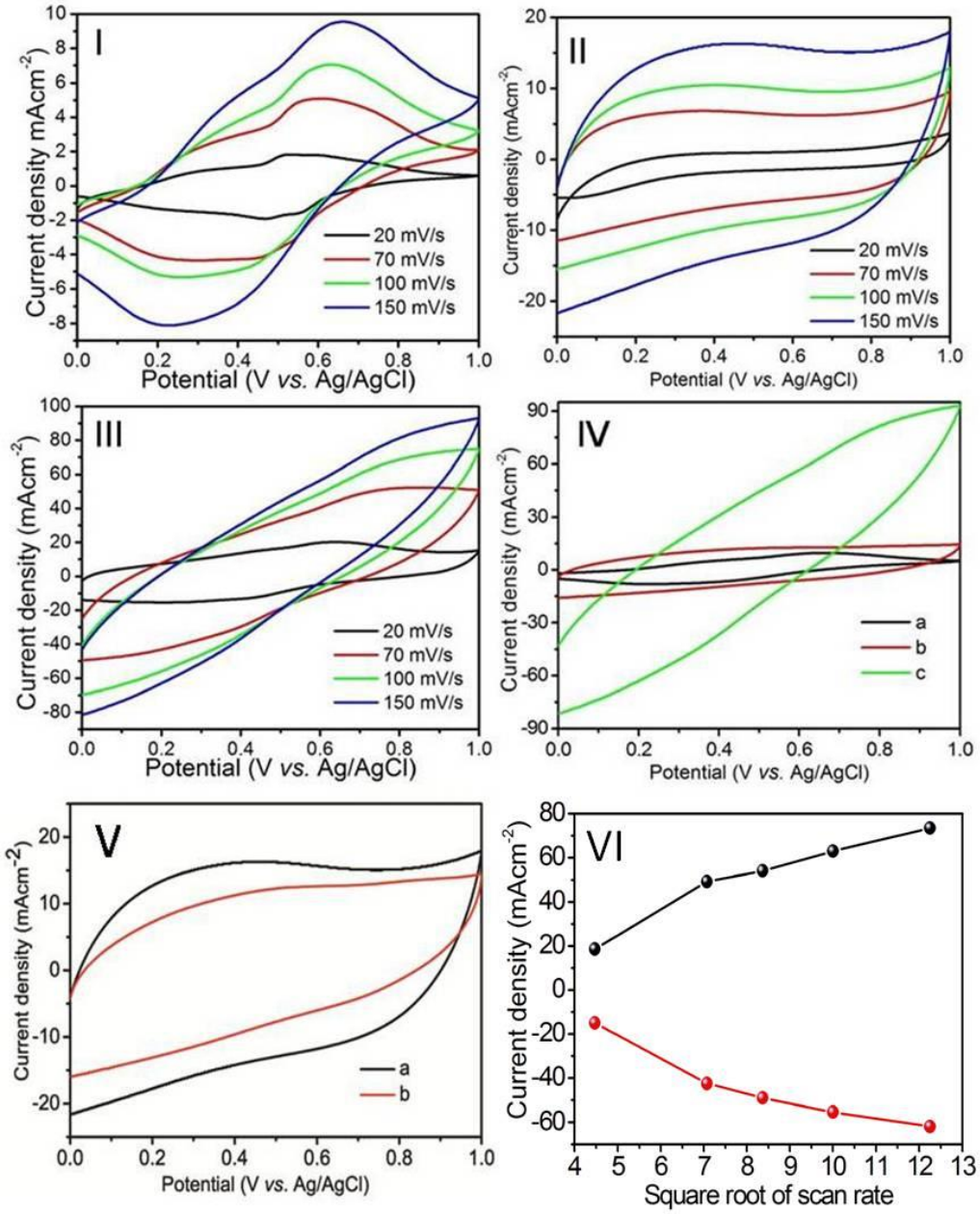

Figure 5.9 CV at different scan rate of (I) PAni, (II) Ox-ECC (III) Ox-ECC/PAni and comparative CV of (IV) (a) PAni, (b) Ox-ECC and (c) Ox-ECC/PAni. (V) comparative CV of (a) Ox-ECC, (b) ECC 800 at scan rate 150 mVs^{-1}in 1.0M H_2SO_4 electrolyte and (VI) current density *vs.* square root of scan rate plot of Ox-ECC/PAni.

In order to investigate the charge storage properties, the GCD experiment was performed in the same experimental condition and corresponding charge-discharge curves are shown in Figure 5.10. In case of Ox-ECC, the CD interval increases with respect to that of ECC800 due to the exfoliation of graphitic sheets on additional functionalities (*see* Figure 5.10(V)). Further, comparing the CD curves of PAni, Ox-ECC and Ox-ECC/PAni at 0.78A/g, Ox-ECC/PAni exhibits longer CD time among others (*cf.* Figure 5.10IV). This is due to the presence of PAni that is capable to reduce the charge conduction path length of defective Ox-ECC and also allowing charge conduction by the diffusion-controlled process. For more understanding, GCD for each material was recorded under various current densities as from 0.78 A/g to 2.89 A/g (Figure 5.10 I-III). The specific capacitance (Cs) *vs* current density of all electrode materials is calculated based on GCD curves using the following equation (1) and tabulated in table 5.2.

$$C_s = \frac{I * \Delta t}{m * \Delta V} \ldots\ldots\ldots\ldots\ldots\ldots\ldots\ldots\ldots\ldots\ldots\ldots\ldots\ldots\ldots\ldots\ldots\ldots (1)$$

where C_s (F/g) is the specific capacitance, I (A) is the applied current, ΔV (V) is a potential window, Δt is time and m (g) is mass of active electrode material loaded on working electrode.

From table 5.2, it is clear that specific capacitances go on decreasing on increasing applied current density.

.

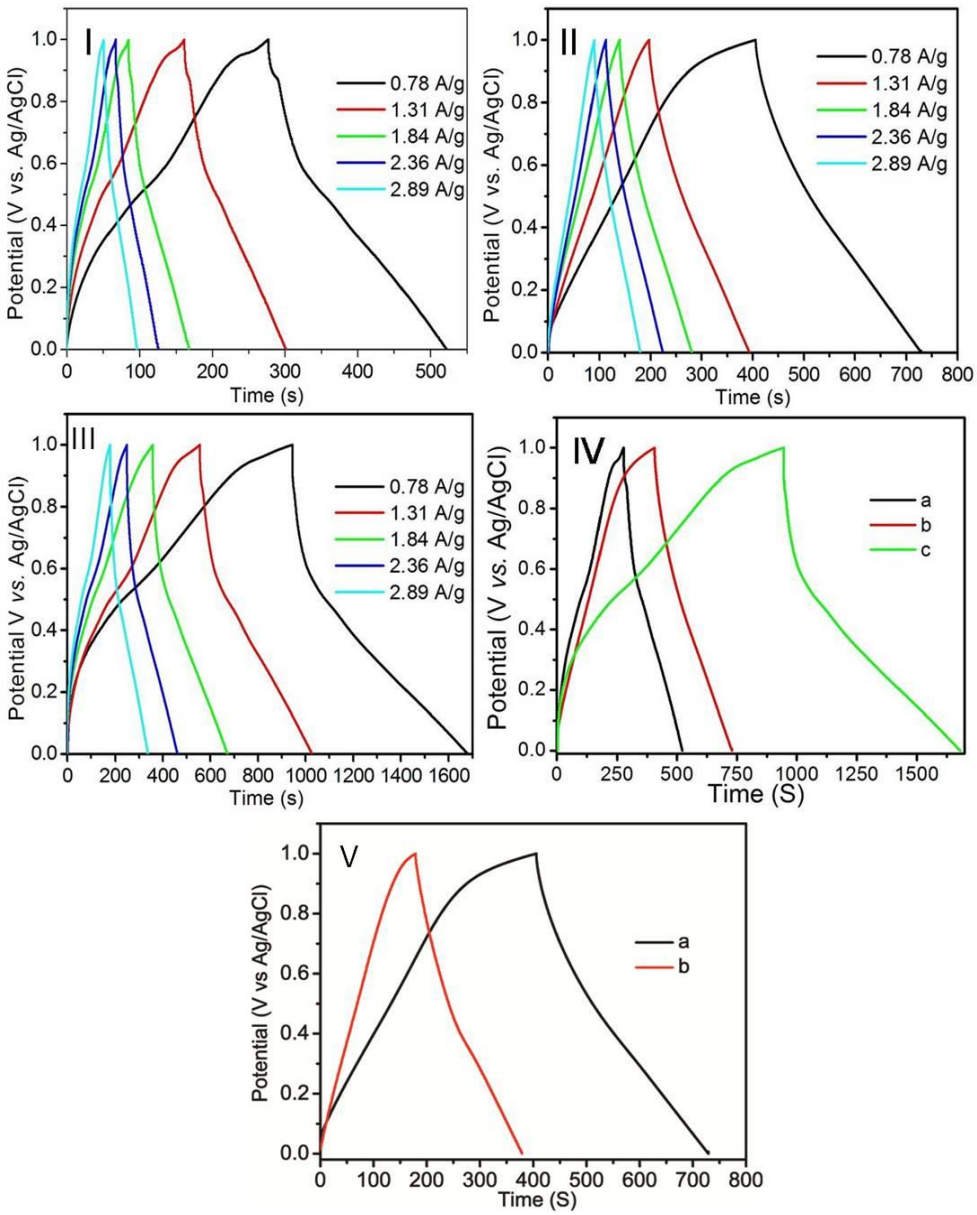

Figure 5.10 GCD of (I) PAni, (II) Ox-ECC (III) Ox-ECC/PAni at different current density and (IV) comparative GCD of (a) PAni, (b) Ox-ECC and (c) Ox-ECC/PAni, (V) comparative GCD of (a) Ox-ECC and (b) ECC 800 at current density 0.78 A/gin 1.0M H_2SO_4 electrolyte.

On further oxidation of ECC800, C_s increases to 569.4F/g due to additional oxygen functionalities which favoring the larger electrolyte interactions and enhancing its performance. However, on the coating of these sheets with PAni, we observe 1542.84

F/g (63% relative increment with respect to Ox-ECC) due to the interconnecting network of PAni over Ox-ECC sheets that reduce the conducting path length of defective Ox-ECC.

EIS was performed for PAni, Ox-ECC and Ox-ECC/PAni in the frequency range from 100 kHz to 10.0 mHz (as shown in Fig.5.11Id-f) and compared with ECC (Fig.5.11Ia-c). The Nyquist plot consists of two regions: the first one is nearly at low frequency showing a vertical straight line, and another a semi-circle (on Z'-axis) like shape appeared at high frequency and inclination of the curve towards Z''-axis is the consequence of high charge accumulation on electrode surface [Subramanya et al. (2015), Kumar et al. (2011)]. PAni is impeding the charges due to its compact surface texture and having a low surface area (Figure 5.11Id) whereas, Ox-ECC has better capacitive behavior than that of ECC 800 (Figure 5.11Ic and Figure 5.11Ie). This is due to more hydrophilicity of Ox-ECC that is favoring more and more electrolyte interactions, still having low surface area [Jin et al. (2013)]. However, Ox-ECC/PAni is showing the vertical straight line is more inclined towards the imaginary axis (Z"-axis) and reveals the better capability to store more charges than other counterparts (Figure 5.11If).

The durability and stability of any catalysts is a critical factor for its real and practical applications. So, in order to exhibit this property, we performed CV for 1000 cycles using an as-modified electrode based on Ox-ECC/PAni material, and retention of capacitances has been calculated for every 50 cycles as shown in Figure 5.11II. From this plot, it can be seen that specific capacitance values are almost constant. The slight variation might be a consequence of an inhomogeneous surface. Finally, we found

88% retention in specific capacitance after 1000 cycles. The morphological textures of modified electrodes are almost the same and polymer coating can be seen after the stability test. It means that the polymer is still intact with the surface of carbons even after this test (*cf.* Figure 5.11IIa and Figure 5.11IIb). Table 5.3 also summarizes comparative research works based on ACs from biowastes and its modification with PAni. From this table, it is concluded that the number of ACs have been developed while ECC derived composite exhibit better performance compared to others.

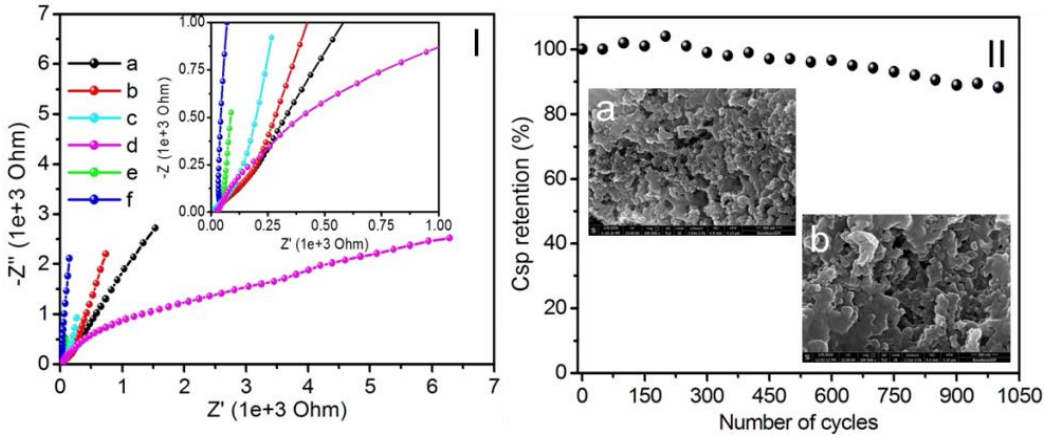

Fig. 5.11: (I) EIS of (a) ECC 600, (b) ECC 700, (c) ECC 800, (d) PAni, (e) Ox-ECC and (f) Ox-ECC800/PAni. Inset shows an enlarged view of a similar curve and (II) Plot of % retention *vs.* number of cycles.

Table 5.2 The specific capacitance of as-synthesized materials at different current densities.

Samples	**Specific capacitance (C_s) (in F/g) at**				
	0.78 A/g	**1.31 A/g**	**1.84 A/g**	**2.36 A/g**	**2.89 A/g**
Ox-ECC800	569.4	549.14	527.04	512.00	502.02
PAni	407.16	399.55	310.96	295.00	283.2
Ox-ECC/PAni	1542.84	1350.61	1232.8	1083.24	979.71

Table 5.3 Comparative capacitive profiles for activated carbons derived from various biomasses reported earlier.

Materials	Current A/g)	Cs (F/g)	**Electr-olyte**	**electrodes Cell**	**References**
Cassava peel waste	0.5	153	0.5M H_2SO_4	3	Ismanto et al. (2010)
Cotton pulp sheet	1.0	107	5.0 M KCl	3	Jiang et al. (2016)
Rice husks	0.1	147	6.0 M KOH	2	Teo et al. (2016)
Carbon Fiber	0.4	180.1	1.0M H_2SO_4	2	Ma et al. (2016)
PAni/RGO/SiO_2	0.2	320	1.0M H_2SO_4	3	Kim et al. (2016)
3D-KSC/SrGO/PAni	0.3	1224	1.0M H_2SO_4	3	Wang et al. (2018)
Ricehusk carbon/PAni	0.2	465	1.0M H_2SO_4	3	Lebedeva et al.(2018)
PAni/cellulose-derived carbon	1.0	765	1.0M H_2SO_4	3	Zhang et al. (2019)
Carbon-PAni	0.1	312	0.1M $NaNO_2$	3	Kumar et al. (2018)
Enteromorphaprolif-era carbon/PAni	1.0	622	1.0M H_2SO_4	3	Du et al. (2017)
Ox-ECC800/PAni	0.78	1582.84	1.0M H_2SO_4	3	Present work

5.4. Conclusions

Random-mesoporous networked Ox-ECC/PAni is synthesized with the expanse of PAni over Ox-ECC surface. Although the surface area decreases but specific capacitance increases from 569.4 F/g to 1542.84 F/g due to the presence of conducting PAni that (a) shorten the conducting path length of defective Ox-ECC and (b) favors charge transfer behavior by the diffusion-controlled process. As-

synthesized Ox-ECC/PAni possesses excellent cycling stability for 1000 cycles that reveals 88% retention in specific capacitances without changing its morphological textures. Importantly, this works gives a new source for the preparation of an electroactive carbon which is cheap, eco-friendly, sustainable, and high electroactive material with additional significance for environmental pollution and waste management.